Journal of Materials Chemistry A

ROYAL SOCIETY OF CHEMISTRY

PAPER

View Article Online
View Journal | View Issue

Cite this: J. Mater. Chem. A, 2025, 13, 6482

An energy efficient and sustainable approach to structural health monitoring in carbon fiber composites: harnessing sound-induced vibration with $Ti_3C_2T_x$ MXene/AgNPs modified P(VDF-TrFE) sensors†

Fatemeh Mokhtari, *[a] Richard W. Symes,[ab] Žan Simon,[c] Bhagya Dharmasiri,[c] Luke C. Henderson,[c] Mathew W. Joosten[b] and Russell J. Varley *[a]

Received 1st November 2024
Accepted 22nd January 2025

DOI: 10.1039/d4ta07797k

rsc.li/materials-a

The growing demand for high-strength, lightweight carbon fiber composites (CFCs) in various industrial sectors highlights the necessity of structural health monitoring (SHM) to prevent catastrophic failures. Accelerometers, as reliable battery-operated monitoring devices, face risks of exposure in harsh environments. Therefore, it is essential to explore a self-powered and highly sensitive alternative sensor. To address this necessity, flexible polymer-based piezoelectrics are gaining attention as self-powered sensors. However, improving their sensitivity in SHM remains a challenge. Here, nanofiber sensors made from a poly(vinylidene fluoride-*co*-trifluoroethylene) (P(VDF-TrFE)) copolymer modified with $Ti_3C_2T_x$ MXene and silver nanoparticles (AgNPs) are fabricated through the electrospinning technique. The introduction of MXene and AgNPs (1 wt%) improves crystallinity by 23% and boosts output voltage nine times, while maintaining good flexibility in an all-fiber-based sensor structure. In an innovative approach, sound-induced vibrations are utilized to stimulate the mounted sensors on various thicknesses of CFCs for SHM. This approach outperforms conventional accelerometers in detecting three types of damage (longitudinal, transverse, and impact) over a frequency range of up to 1500 Hz. This strategy not only effectively harnesses environmental sound in an energy-efficient way but also demonstrates sensor sensitivity, highlighting its potential to advance smart sensing systems.

1. Introduction

Carbon fiber composites (CFCs) offer superior high specific strength, lightweight properties, and high corrosion resistance, enabling advancements across multiple engineering sectors, including aerospace, automotive, renewable energy, construction, sports and medical equipment.[1,2] However, low damping, along with exposure to long-term vibrational environments, makes carbon fibres susceptible to fatigue damage such as cracks and delamination. One of the most concerning types of composite damage is impact damage caused by low-velocity impacts from bird strikes, hail, gravel, or accidental tool drops.[3] These impacts may not leave visible signs of damage but can propagate, decrease performance, reduce service life, and eventually cause failure. Therefore, the use of structural health monitoring (SHM) is crucial for continuous real-time condition assessment and damage detection, ensuring the safety, longevity, and reliability of composite structures through continuous, non-destructive monitoring techniques.[4] By offering early warning of potential failures, SHM can help prevent disasters and lowers maintenance costs, extending the service lifetime of structures and minimizing downtime.[5]

SHM can use a range of techniques including ultrasound inspection,[6] acoustic emission,[7] strain measurement,[8] and modal analysis[9] but they must be highly sensitive, reliable, and cost-effective. Many sensors rely on external power sources such as chemical batteries or wired power grids, leading to increased monitoring costs, operational complexity, and environmental pollution risks.[10,11] Therefore, innovative sensor technologies that convert renewable and waste energy into electrical signals for monitoring are increasingly in demand.[12]

Piezoelectric sensors with the capability of converting mechanical vibrations into electrical signals are highly suitable for SHM because of their compact size, lightweight design, and cost-effectiveness.[12,13] These features make them particularly

[a]Carbon Nexus at the Institute for Frontier Materials, Deakin University, Waurn Ponds, Victoria 3216, Australia. E-mail: fatemeh.mokhtari@kuleuven.be; russell.varley2@rmit.edu.au

[b]School of Engineering, Faculty of Science Engineering and Built Environment, Deakin University, Waurn Ponds, VIC 3216, Australia

[c]Institute for Frontier Materials, Deakin University, Waurn Ponds, Victoria 3216, Australia

† Electronic supplementary information (ESI) available. See DOI: https://doi.org/10.1039/d4ta07797k

effective for composite health monitoring of aircraft,[14] wind turbine blades,[15] bridges,[16] and automotive applications.[17] There are two operational modes for piezoelectric sensors, the d_{33} mode, which corresponds to the piezoelectric effect when the electrical charge is generated in the direction of the applied mechanical stress, typically along the axis of the crystal. This makes d_{33} ideal for measuring compression, as it is sensitive to changes in pressure or axial stress within a structure. On the other hand, the d_{31} mode represents the charge generated when mechanical stress is applied perpendicular to the polarization direction, meaning that it is most sensitive to vibrations. Therefore, d_{31} is commonly used for vibration sensing and is mostly considered for SHM analysis.[18] Piezoelectric sensors in SHM are widely used for modal analysis-based methods due to their ease of measurement and compatibility with data acquisition systems. As damage occurs in a structure, its vibrational frequencies change, which also affects signals from piezoelectric sensors.[19]

PZT (lead zirconate-lead titanate) piezoelectric sensors have been used as strain sensors for damage monitoring in composite structures,[20] particularly in the 0–250 Hz frequency range for operational modal analysis. However, due to the brittle nature of ceramics, they are limited in size and cannot easily be mounted on curved or flexible structures.[21] Ceramic piezoelectric sensors are highly sensitive, but the brittleness of PZT sensors can cause them to fail prematurely. This can result in sensor deterioration before it can detect any damage, especially in carbon fiber composites.

Polymeric piezoelectric sensors are advantageous for SHM due to their removability and reusability without affecting performance, making them ideal for composite health monitoring.[22] Among piezo polymers, polyvinylidene fluoride (PVDF) has excellent piezoelectric properties and is considered a self-powered sensor with low-cost, high chemical resistance, thermal stability, and flexibility. These qualities make it a compelling alternative to piezoelectric ceramics.[23,24] PVDF film sensors are flexible and easy to shape and can be mounted with double-sided adhesives. While a pure PVDF film has been successfully used for monitoring radar tower vibrations, it requires preamplifiers that are prone to damage from humidity. This can lead to short circuits or electromagnetic interference (EMI), which may corrupt the signal by damaging the transistors.[25] Therefore, the performance of PVDF-based polymers must be optimized to eliminate the need for an external amplifier. This will enable self-powered operation, where the sensor generates enough voltage without amplification to accurately determine the modal properties of a structure.

The PVDF copolymer, poly(vinylidene fluoride-*co*-trifluoroethylene) (P(VDF-TrFE)), exhibits higher piezoelectric constants due to its enhanced ability to crystallize in the β-phase. The added fluorine atoms from TrFE units disrupt the formation of the α-phase (tgtg′ conformation) promoting crystallization of the all-trans conformation, which is key to β-phase formation.[26] Although P(VDF-TrFE) copolymers primarily crystallize in the β phase, achieving a strong piezoelectric response remains challenging. While the presence of the β phase is essential, it is not sufficient to maximize the piezoelectric performance.[27] Therefore other strategies including adding piezo ceramics and conductive and two dimensional (2D) fillers have been explored.[28]

In the electrospinning process, incorporating conductive fillers into polymer solutions can enhance the electric field strength, resulting in increased polymer dipole polarization at a constant voltage.[29] MXenes (formula: $M_{n+1}X_nT_x$, where M = early transition metal, X = carbon and/or nitrogen, $n = 1$–4, and T_x = –F, –O, –OH) have attracted a great deal of interest for their unique properties, such as excellent electrical conductivity, energy storage, and electrochemical reactivity.[30] Two dimensional ($Ti_3C_2T_x$) MXene has superior conductivity to increase the dielectric constant, charge-inducing, and charge-trapping capability of piezoelectric polymers.[31,32] MXene flakes induce polarization locking in P(VDF-TrFE) and enhance electromechanical performance. The polar groups (–OH and –F) on the MXene surface interact with C–H and C–F bonds in the P(VDF-TrFE) matrix. This interaction, facilitated by the MXene layered structure, results in self-polarization.[33,34]

The interaction between silver nanoparticles (AgNPs) and fluorine atoms in PVDF-based polymers enhances piezoelectric properties and boosts β-phase formation (~80%), resulting in nanofibers with improved electrical conductivity and polarization during electrospinning.[35] Incorporating MXene/AgNPs into P(VDF-TrFE) composites provides significant EMI shielding properties, allowing the sensor to have less noise and higher sensitivity. The introduction of AgNPs and MXene flakes with ultra-high conductivity has helped develop robust conductive channels for charge transfer in piezoelectric sensors, making it an effective strategy for multifunctional sensing technology. Recently it has been shown that a PVDF/AgNP/MXene composite nanofibrous film with enhanced piezoelectric performance was successfully fabricated using near-field electrospinning. The incorporation of MXene and AgNPs significantly boosted the electrical conductivity of the PVDF-based composite, leading to improved piezoelectric properties.[36]

Many researchers have explored various piezoelectric nanocomposites to harness environmental sound energy, demonstrating its potential for powering low-energy devices and addressing noise pollution.[37–39] The aim of this work is to demonstrate the potential of high-performance piezoelectric sensors to harness vibrations induced by environmental sound for SHM of carbon fiber composites. To do this, the effect of varying levels of AgNP loading (0, 0.5, 1, and 2 wt%) in the P(VDF-TrFE)/$Ti_3C_2T_x$ MXene nanofibers was investigated. Piezoelectric sensors were fabricated through electrospinning and then FTIR, XRD, and DSC analysis provided insights into the structure and crystallinity of the nanofibers. The electromechanical conversion performance of the piezoelectric sensors was compared using both compression and vibration modes. An optimized sensor for detecting sound-induced vibrations was established, and SHM tests were performed on three types of artificial damage (longitudinal, transverse, and impact) on CFCs to assess the sensor sensitivity in damage detection.

2. Materials and methods

2.1. Materials

The P(VDF-TrFE) powder (Piezotech FC25, France) was purchased from the Arkema Group. AgNPs were supplied from Inframat Advanced Materials Co., Ltd, USA. The Ti_3AlC_2 precursor was purchased from Carbon-Ukraine Ltd. Lithium fluoride (LiF, 99% purity), hydrochloric acid (HCl, 12 M), acetone, and *N*,*N*-dimethylformamide (DMF, ≥99%) were purchased from Sigma-Aldrich Pty Ltd. All chemicals were used as received, without further purification. $Ti_3C_2T_x$ MXene was synthesized using the minimally intensive layer delamination (MILD) technique resulting in single-layer MXene flakes as described in our previous work.[40]

2.2. Sensor fabrication

Acetone was added to the DMF solution in a 6 : 4 mass ratio. Subsequently, AgNP powder (0, 0.5, 1, and 2 wt%) was incorporated into the solution and sonicated for 1 hour. Afterward, MXene (0.1 wt%) and P(VDF-TrFE) (10 wt%) powder were introduced, and the mixture was stirred at 60 °C for 6 hours to achieve a homogeneous solution for electrospinning. The electrospinning process was carried out at 18 kV, with a feed rate of 0.8 mL h^{-1} on silver-coated nylon fabric as electrodes. The distance between the needle and the collector was set at 15 cm, and a grounded rotating drum (100 rpm) was used as the fiber collector. The electrospun webs were cut into 3 × 3 cm squares and secured with Kapton tape. Copper wires (0.25 mm) were stitched to both electrodes for signal measurements.

2.3. Fabrication of carbon fiber composites and creation of artificial damage

Twill carbon fiber (standard modulus, 320 g per sq m) reinforced epoxy-amine composites were fabricated using a wet lay process. Resin RIM 935/hardener 936 was mixed and degassed under vacuum. Each ply of the carbon fibre was wetted out with resin; the layers were then stacked and carefully rolled to eliminate any voids, then vacuum-bagged, debulked, and cured in a pre-heated convection oven at 80 °C for 16 hours under vacuum. Composite samples were then cut from each plate using a wet diamond saw to dimensions of 51 mm × 331 mm. To evaluate sensor performance, three samples with artificial damage were prepared. Longitudinal and transverse damage were created by cutting a 20 mm long slit through the sample with a knife, and impact damage was created using a center punch to make a 5 mm diameter circular hole in the sample. The artificial damage and experimental setup are shown in Fig. 1.

The carbon fibre composites were clamped in a cantilever condition with one end fixed in a vice while the other is allowed to vibrate freely. A 3 W USB speaker was employed to excite vibrations in the carbon fibre composites. The piezoelectric sensor was connected directly to an MCCDAQ USB1808X with the electrodes connected as a differential pair to reduce EMI pickup from the cables. An ADXL356C accelerometer was used as a reference sensor on the same data acquisition system. The accelerometer was powered using an external 3.3 V power source for the required internal amplifiers. All measurements were conducted at 20 000 samples per second to provide a sufficiently high Nyquist frequency and reduce aliasing effects at the excitation frequencies.

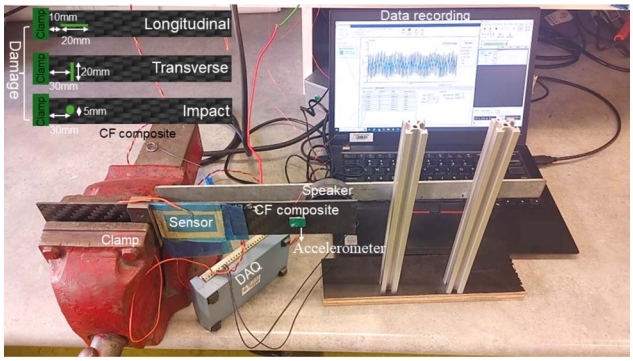

Fig. 1 Experimental setup for structural health monitoring of carbon fiber composites to detect three types of artificial damage.

2.4. Characterization

FTIR spectroscopic analysis was conducted using a Bruker Lumos (Bremen, Germany) in ATR mode. Differential scanning calorimetry (DSC) was carried out using a Netzsch DSC 214 Polyma instrument. The mechanical properties of the samples were evaluated using an Instron universal testing machine equipped with a 50 N load cell, applying a tensile strain rate of 2 mm min^{-1}. Scanning electron microscopy (SEM) images were captured with a Supra 55-VP field emission scanning electron microscope (Zeiss, Germany). The surface morphology of the nanofibers was analyzed using a field emission scanning electron microscope (JEOL JSM 7800F) at 3 keV. Fiber diameter measurements were obtained from the SEM images using ImageJ software. Energy-dispersive X-ray spectroscopy (EDX) was conducted using an EDX detector (Oxford Instruments) with Aztec software. The phase structure was characterized by X-ray diffraction (XRD) with a PANalytical XPert Powder system utilizing Cu Kα radiation.

3. Results and discussion

3.1. Morphology and crystallinity of electrospun webs

In this work, single-layer MXene ($Ti_3C_2T_x$) flakes were synthesized through the minimally intensive layer delamination (MILD) technique.[41] Previous work has shown that the optimized MXene concentration for high piezoelectric performance is 0.1 wt%.[40] Thus, in this work, the MXene concentration is kept constant at 0.1 wt% while the AgNP concentration is varied (0.5, 1, and 2 wt%). Fig. 2a shows the prepared solutions for the electrospinning process. After high-speed centrifugation, the water in the MXene solution was replaced with DMF and was sonicated for 1 h. The resulting MXene solution appeared black due to $Ti_3C_2T_x$ flake content. Following the addition of P(VDF-TrFE) and AgNPs and magnetic stirring for 6 hours, the black solution changed to a black-gray hue. The obtained electrospun

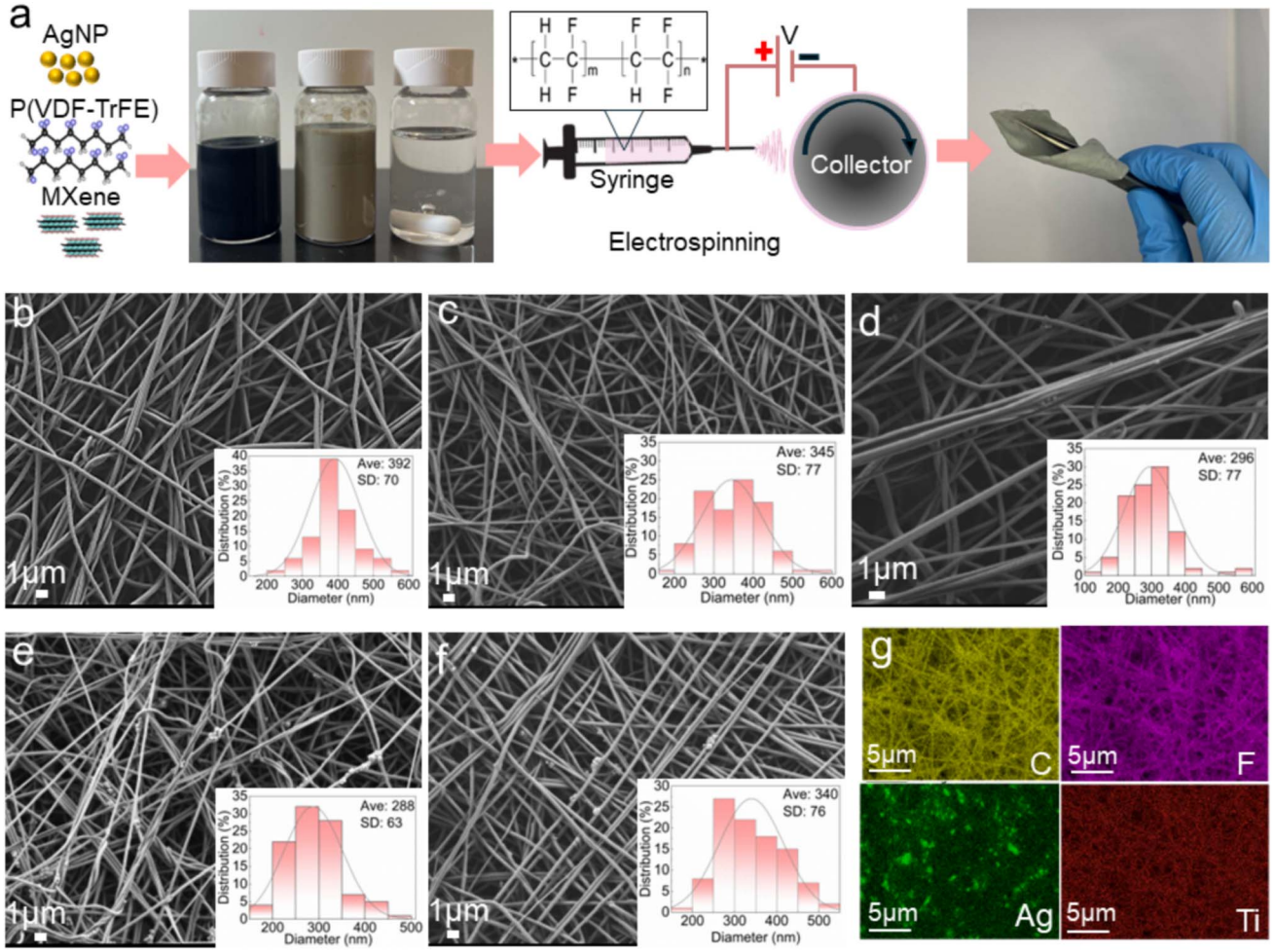

Fig. 2 (a) Fabrication process of electrospun nanofiber of P(VDF-TrFE)/MXene/AgNPs, the SEM image of the as-fabricated P(VDF-TrFE) nanofibers containing (b) P(VDF-TrFE), (c) MXene-0.1 wt%, (d) MXene/AgNP-0.5 wt%, (e) MXene/AgNPs (1 wt%) and (f) MXene/AgNPs (2 wt%), and (g) EDS image of the P(VDF-TrFE) nanofibers containing MXene/AgNPs (1 wt%).

web from these solutions was flexible enough to allow sequential bending, stretching, and twisting. Fig. 2b–f display the SEM morphology images of P(VDF-TrFE)/MXene fibers with different AgNP concentrations. As the AgNP content increased, the nanofiber diameters decreased from 392 nm to 288 nm, due to the enhanced electrical conductivity. The incorporation of MXene and AgNPs as conductive fillers increased charge density and the static electric field force, thereby strengthening the extensional flow of P(VDF-TrFE) molecules and resulting in thinner fibers during the spinning process. SEM images confirmed that agglomeration occurred when the AgNP content reached 2 wt% and bulges and surface roughness appeared on the web due to uneven distribution.[42] This is attributed to the electric charge generated on P(VDF-TrFE) during the electrospinning process exerting a repulsive force on the Ag nanoparticles. Consequently, these particles were observed to deposit within the volume of the nanofibers due to the repulsive force of the electric charges induced on P(VDF-TrFE).[43]

The AgNPs (1 wt%) in the P(VDF-TrFE)/MXene solution enhanced the interaction between AgNPs and P(VDF-TrFE), preventing agglomeration and producing homogeneous nanofibers with EDS analysis (Fig. 2g) confirming the uniform distribution of the target elements (Ag, C, F, and Ti). Ti, the primary element in MXene, is evenly dispersed throughout the matrix without any observable aggregates, further indicating that MXene is well-dispersed in the P(VDF-TrFE) nanofiber.

MXene flakes with average thickness 6 nm (Fig. 3a) were mixed with polymer solution. The XRD patterns in Fig. 3b indicate formation of MXene flakes by successful exfoliation of bulky MAX. This is evidenced by the disappearance of the strong diffraction peak of MAX at $2\theta = 39°$ and the shift of the (002) peak to a lower angle ($2\theta = 6.9°$).[40,44] The XRD spectra in Fig. 3c illustrate the varying crystallinity of the fibers with different AgNP contents. Sharp peaks at 20° correspond to the enhanced (110/200) ferroelectric β phase reflection in P(VDF-TrFE).[45] MXene flakes exhibited a strong peak at $2\theta = 6.9°$ corresponding to the (002) plane of $Ti_3C_2T_x$ MXene.[46] The AgNPs showed peaks at 2θ values of 38.1° and 44.1° corresponding to the face-centered cubic structure with crystal planes for AgNPs at (111) and (200).[47]

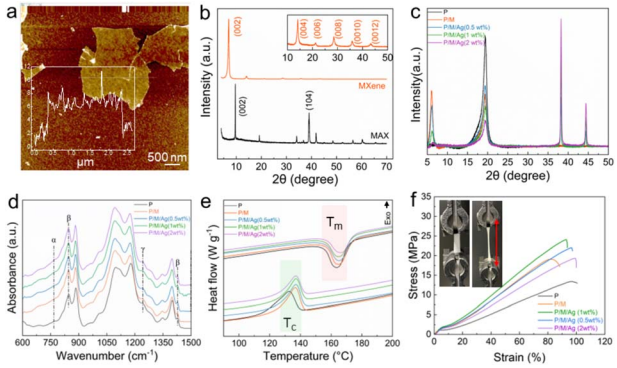

Fig. 3 (a) Atomic force microscopy (AFM) image of MXene flakes deposited on a silicon substrate, (b) X-ray diffraction patterns of Ti_3AlC_2 (MAX phase) powders and pure MXene, and characterization of the electrospun nanofiber web with various contents of AgNPs, P(P(VDF-TrFE)), P/M (P(VDF-TrFE)/MXene), and P/M/A (P(VDF-TrFE)/MXene/AgNP): (c) XRD pattern, (d) FTIR spectra, (e) DSC heating profile and (f) tensile stress–strain curves.

The FTIR spectra of P(VDF-TrFE) nanofibers with MXene and AgNPs showed characteristic peaks of the β-crystalline form at 840 cm^{-1} highlighting the induced crystallization by MXene for P(VDF-TrFE) (Fig. 3d).[48] The FTIR spectra of silver nanoparticles also exhibited prominent peaks at 1384 cm^{-1}.[49]

Fig. 3e presents the DSC melting curves of P(VDF-TrFE) nanofibers with varying AgNP concentrations. The unmodified and modified P(VDF-TrFE) fibers exhibit an endothermic transition between 160 and 166 °C, shifting to higher temperature as the MXene and AgNP concentrations increased. This further complements XRD and FTIR, emphasizing the nucleation efficiency of the nanofillers. When samples are cooled from the melt, the crystallization temperature (T_c) is 132.6 °C for pure P(VDF-TrFE) and 137 °C for the MXene and 2 wt% AgNPs. The increase in T_c with higher filler loading indicates heterogeneous crystallization, leading to smaller crystal sizes, while the narrowing of the T_c peak suggests a more uniform crystalline size distribution.[50] In general, incorporating fillers into semi-crystalline polymer matrices raises the crystallization temperature enhancing the rate of nucleus formation. According to DSC measurements, the P(VDF-TrFE) nanofiber had a crystallinity of 53.4%, while, in contrast, the crystallinity of the nanofiber increased to 59.5% after doping with MXene and further increased to 65.65% with the addition of 1 wt% AgNPs.

MXenes with high moduli enhance the strength and rigidity of the composite, thereby improving its mechanical performance. MXene flakes, with their high aspect ratios, contribute to better reinforcement due to their larger surface area, which facilitates improved interaction with the polymer matrix. Adding MXene is beneficial when the goal is to achieve high moduli and tensile strength in the nanocomposites, rather than maximizing elongation at break.[51] A comparison of the stress–strain curves of various electrospun nanofibers reveals that integrating MXene as a filler results in enhanced mechanical properties by increasing tensile strength by ~two times. This increment is due to the interactions of –F and –OH bonds on the surface of MXene sheets with the C–F and C–H bonds of the P(VDF-TrFE) molecules. Another reason could be the uniform dispersion of AgNPs in the nanofibers, which helps dissipate stress when the fibers are stretched, thereby enhancing the tensile strength.[52] By incorporating 1 wt% AgNPs, the uniform dispersion of the powder in the nanofiber, along with its strong interaction with P(VDF-TrFE), results in an 11% increase in Young's modulus and raises the tensile strength of P(VDF-TrFE) electrospun webs from 13 to 24 MPa (Fig. 3f). However by adding 2 wt% AgNPs, due to agglomeration, this filler acts as a defect in the structure and its tensile strength decrease (Fig. S1†). The overall decrease in elongation is attributed to the MXene/Ag content that acts as stress concentration and limited the degree of deformation of the polymer molecular chain.[53,54] However, with precise adjustment, it is possible to achieve a balance between tensile strength and elongation.

3.2. Electromechanical conversion performance of piezoelectric sensors in compression

Fig. 4a illustrates the fabricated sensor with conductive silver-coated nylon fabric on both sides serving as the electrodes to collect the generated charge in compression mode (d_{33}).

To test the inherent piezoelectricity of piezoelectric polymers and eliminate the triboelectric effect during the compression test, it is important to prevent any interfacial friction between the piezo polymer and electrodes, as well as between the testing apparatus and the fabricated sensor in compression modes. To avoid surface charges and the triboelectric effect, electrospinning was performed directly on silver-coated fabrics as electrodes, ensuring that there was no gap between the active polymer and the electrodes. Additionally, the sensor was fixed with Kapton tape on one side of the testing apparatus, with a preload of around 2 N applied to prevent any slipping.[55] A maximum force of 34 N was selected as the highest force that our setup could apply to the sensor in order to generate the maximum output voltage. Under the constant pressure and at a frequency of 1 Hz (Fig. 4b and c), the output voltage initially increases and then declines as the AgNP concentration increases, reaching a maximum peak of ~0.9 V for the sensor containing 1 wt% Ag (Fig. 4d). This behaviour is attributed to the inclusion of AgNP and MXene-based fillers, which boost the dielectric constant, enhancing the electrical properties of the sensor. As the AgNP filler concentration increases, the sensor conductivity increases until a percolation threshold is reached. Beyond this point, additional conductive pathways cause charge leakage rather than accumulation, reducing charge separation efficiency.[56]

The asymmetric characteristic between the output positive and negative voltage signals of the sensors could be attributed to the lag of the charge transfer cycle relative to the deformation of the active materials[57] and also strain rate[58] in pressing and release cycles. The asymmetric voltage between the positive and negative values observed in the soft and flexible piezoelectric sensor (1 wt% AgNP) in compression mode primarily results from the deformation of the electrospun web and the charge generation mechanism. Each peak of positive and negative

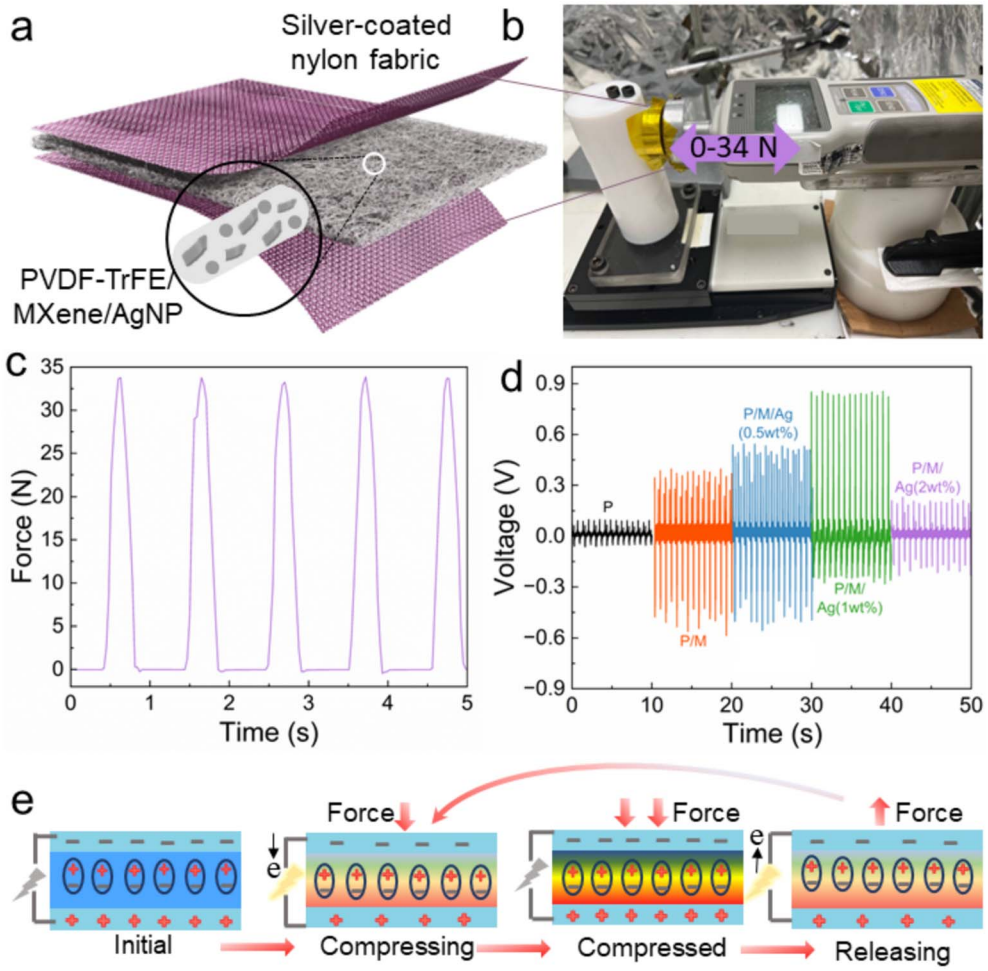

Fig. 4 (a) Schematic illustration of the electrospun P(VDF-TrFE)/MXene/AgNP sensor, (b) cyclic pressure of the sensor in compression mode, and (c) loading profile applied using a dynamic tester at 1 Hz from 0 to 34 N. (d) Output voltages of the nanofiber sensors with various concentrations of AgNPs, and (e) schematic illustration of the piezoelectric sensor mechanism in charge generation.

corresponds to the compression and release of force in each cycle. For the 1 wt% AgNP sensor, the thinner fibers allow for more fibers to be present within the same thickness. As a result, during compression, the material exhibits greater flexibility, leading to higher voltage generation in the pressing cycle. However, during the release cycle, the structure may become more densely packed, preventing the fibers from returning to their original positions or having a delay in returning, which results in a lower output voltage during release.

Fig. 4e shows the general mechanism and process of the piezoelectric effect. When no external force is applied, the sensor has no output due to electrical equilibrium. By applying pressure, the dipole moment generates an electrical potential difference between the top and bottom electrodes. When the force is released, electrons return to their equilibrium state under short-circuit conditions.[26] In summary, the fabricated sensors demonstrate optimal electrical output capability with an active area of 7 cm^2, a pressure of 34 N, and a frequency of 1 Hz, generating a voltage of 0.9 V.

3.3. Electromechanical conversion performance of piezoelectric sensors in vibration

To evaluate the performance of the fabricated sensor in various concentrations of AgNPs under vibration, a test was performed using a sinusoidal base excitation with an input acceleration of 49 ms^{-2} at 1500 Hz. This loads the base beam at high frequency in bending, with the sensors mounted on the surface of the carbon fiber composite beam, where they are loaded in tension with the voltage measured (Fig. 5a) across the thickness of the sensor (d_{31} mode). As can be seen, the sensor with 1 wt% AgNPs shows the highest sensitivity for vibration measurement which is aligned with the PFM results (Fig. S2†). Also, the maximum output voltage of sensors in mode d_{33} is higher than that in mode d_{31}, due to higher piezoelectric coefficients of P(VDF-TrFE) in this mode ($d_{33} \approx -30$ pC N^{-1} and $d_{31} \approx 25$ pC N^{-1}).[59] According to eqn (1), the piezoelectric coefficient is correlated with output voltage, where V is the output voltage, d_{31} is the piezoelectric coefficient, t is the sensor thickness, σ is the applied stress and C is the capacitance of the sensor.[60]

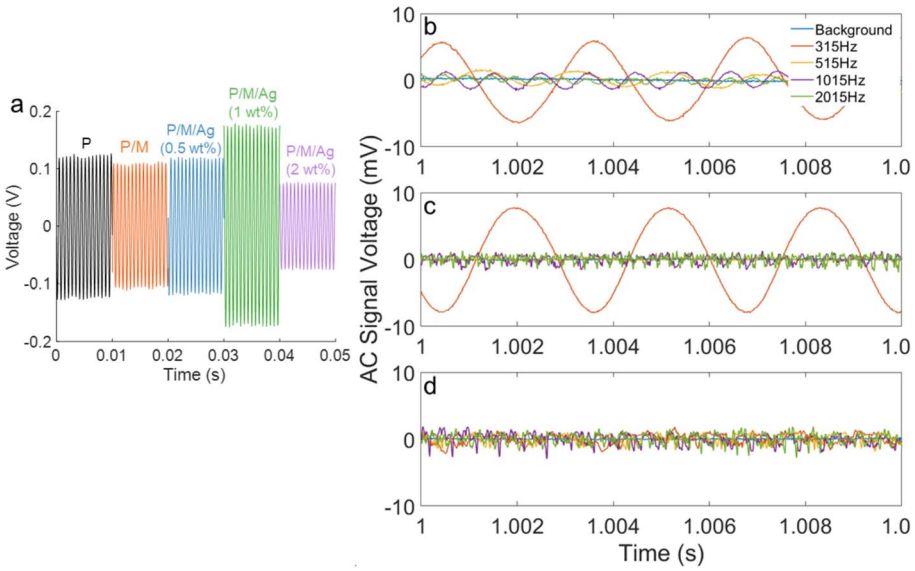

Fig. 5 (a) Output voltage of piezoelectric sensors with various concentrations of AgNPs under a vibration loading of 1500 Hz on the carbon fiber composite beam, and piezoelectric sensor output voltage with DC offset removed at sound frequencies 315, 515, 1015, and 2015 Hz, for different carbon fibre composite thicknesses of: (b) 0.44, (c) 2.4, and (d) 3.15 mm.

$$V = d_{31} \times \sigma \times \frac{t}{C} \quad (1)$$

Carbon fiber composites with three different thicknesses (0.44, 2.4, and 3.15 mm) were exposed to sound frequencies ranging from 315 to 2015 Hz to optimize the composite thickness for the fabricated sensor. The sensor fabricated with 1 wt% AgNPs was chosen for future exploration, as it showed the highest output voltage (Fig. 5a). The sensor was attached to the carbon fiber composites, as shown in Fig. 1, to measure the strain caused by sound-induced vibrations. Fig. 5b shows that the generated signals from the sensor are the clearest for the thinnest CFC (0.44 mm), generating a 5.8 mV output voltage. Indeed, the vibrational signal in this case is distinct from noise at all tested frequencies, confirming the suitability of the sensor design for this thickness. Fig. 5c demonstrates the vibration response at a composite thickness of 2.4 mm. The excitation frequency of 315 Hz shows a very high signal amplitude due to the excitation frequency being close to one of the CFC beam natural frequencies of 308 Hz, magnifying the response (Fig. S3†). At the other tested frequencies, the vibration signal is indistinguishable from noise. Similarly, for a beam thickness of 3.15 mm, the signals are dominated by noise (Fig. 5d).

The power spectral density (PSD) at the excitation frequency was considered a factor to quantitatively compare sensor sensitivity for different composite thicknesses (Table 1). The PSD decomposes the energy of the signal contained in a frequency component, eliminating noise that is not at the excitation frequency and caused by other excitation sources or measurement noise. Fig. 5 and Table 1 confirm that the sensor for the carbon fiber composite with a thickness of 0.44 mm shows a higher sensitivity to sound-induced vibrations across all tested frequency ranges and was selected for further modal and SHM analysis (Fig. S4–S6†). The coupling efficiency between air and solid materials is inherently low, which leads to reduced energy transfer and consequently low-amplitude vibrations. Therefore, the piezoelectric sensors need to exhibit high sensitivity to generate reliable signals. This confirms the sensitivity of the fabricated piezo sensor in detecting these frequencies at a CFC thickness of 0.44 mm effectively.

3.3.1. Comparison of piezoelectric sensors and accelerometers for modal analysis. Accelerometers are motion-based sensors used to capture the vibration response of composite structures for modal analysis. Accelerometers are widely used for SHM applications; however, commonly used IEPE (Integrated Electronics Piezo-Electric) accelerometers have the

Table 1 Power spectral density from piezoelectric sensors at sound frequencies of 315, 515, 1015, and 2015 Hz for various thicknesses of carbon fiber composites

Carbon fiber composite thickness (mm)	Power spectral density (V^2/Hz)			
	315 Hz	515 Hz	1015 Hz	2015 Hz
0.44	3.50×10^7	1.20×10^6	1.32×10^6	1.71×10^6
2.4	6.01×10^7	2.40×10^4	2.91×10^3	5.35×10^3
3.15	8.37×10^4	1.74×10^4	1.65×10^4	1.01×10^5

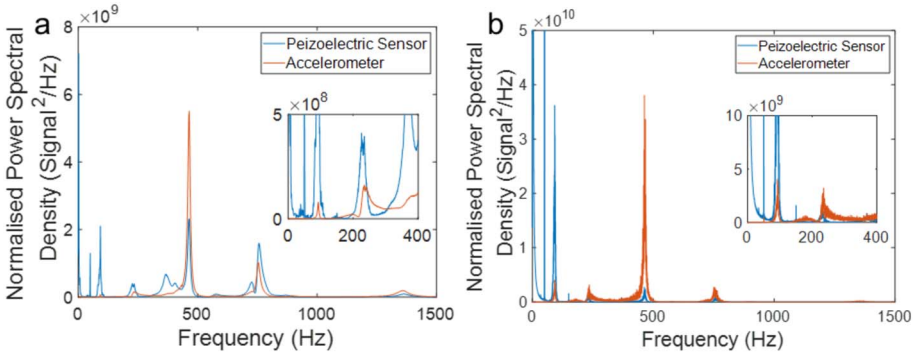

Fig. 6 The output power spectrum of the piezoelectric sensors and accelerometer under (a) sweep and (b) pink noise excitation. Each voltage signal was normalized to the root mean squared voltage prior to processing.

disadvantage of being expensive for SHM applications which limits the size and prevalence of systems.[61] The use of low-cost MEMS (micro-electro-mechanical sensors) combined with low-cost piezoelectric film sensors has the potential to create new low-cost SHM approaches for civil applications such as bridges,[62,63] skyscrapers,[64,65] large structures,[66] and military aviation.[67]

In experimental modal analysis, a measured input force is used to excite vibrations in a structure, allowing for the frequency response function (FRF) to be calculated to measure the structure response to the input. Most SHM applications do not use a measured input as an operational vibration source. These can originate from internal sources such as motors or from external sources during operation, such as road noise, wind or sound.[68] To compare the performance of the piezo sensor and the accelerometer, both were exposed to sweep and pink noise signals (Fig. 6). To test the use of the piezo sensors for SHM using sound induced vibration, both a sweep and a random noise spectrum were tested from 0 to 1500 Hz. The sweep excitation (Fig. 6a) provides a clear frequency power spectrum as the structure is excited by only a single frequency each time. However this type of excitation is rarely encountered in SHM as natural vibration and sound sources are generally wide bands exciting all frequencies simultaneously. A pink noise (Fig. 6b) distribution was used to mimic operational vibration sources, as it is a good approximation for environmental noise in many cases.

In modal analysis, the natural frequencies of the structure can be used to determine stiffness. The frequency response of the piezo sensor and the accelerometer are similar, with both showing peaks at 1356, 756, 464, 234, and 92 Hz that correspond to the bending modes of the tested sample. This similarity demonstrates the effectiveness of the piezo sensors for SHM. The 50 Hz peak observed in Fig. 6a and b for the piezo sensor is attributed to electromagnetic interference pickup, which is reduced in the accelerometers using internal voltage regulators and amplifiers. In the zoomed-in view, the relative response of the piezo sensors is higher at low frequencies compared to the accelerometers. The magnitude of the power spectral density for the accelerometer is larger due to the internal amplification of the acceleration signal. In the piezoelectric sensor spectrum in Fig. 6a, additional peaks at 368 and 579 Hz can be observed, which do not appear in the accelerometer spectrum. These peaks correspond to twisting modes of the CFC beam, as the motion of the composite will be minimal at the centerline of the sample, where the accelerometer is placed and the measured response from the accelerometer will be low. This can also be seen in Fig. 7; in modes one, two and

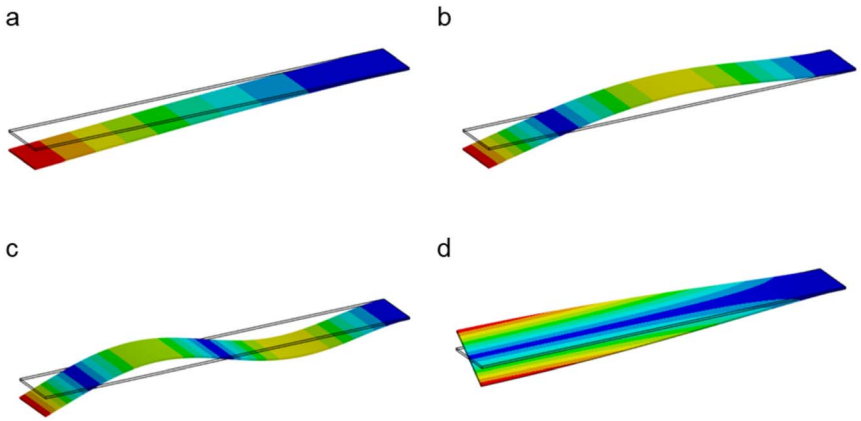

Fig. 7 A finite element simulation showing the vibration mode shapes (maximum deflection) for the first 4 modes of the CFC beam: (a) first bending mode, (b) second bending mode, (c) third bending mode, and (d) first twisting mode.

third (Fig. 7a–c) the deflection of the sample is large at the accelerometer location and the strain at the clamped portion of the beam is also maximum. In the twisting mode (Fig. 7d) along the centre line there is no motion; however the strain at the clamp is still high allowing for the piezoelectric sensors to detect these vibrations while it remains undetectable for the accelerometer.

Comparison between the performance of the fabricated sensor and accelerometer confirms that the flexible piezoelectric sensor containing 2D MXene and 1 wt% AgNPs is sensitive enough to show a clear response to low-amplitude sound-induced vibrations without the need for external power sources.

3.4. Damage detection using the piezoelectric sensor

This section demonstrates the ability of the fabricated sensor to detect three types of damage, including longitudinal, transverse and impact (Fig. S7†). To perform this test, sound-induced vibrations were measured over an extended frequency period to generate a high-resolution spectrum and minimize noise (Fig. 8a). Changes in the natural frequencies of vibration between the undamaged and damaged composite beams seen in the power spectra indicate alterations in the properties of the underlying composite structure.

Fig. 8a shows the spectra for each of the CFC beams. Due to damage in three of the beams, a noticeable change in the structure response is observed. The vibration modes of damaged beams are generally more complex due to changes in stiffness along the beam length and the possible nonlinear response of damaged areas of the structure. At low frequencies of 60–100 Hz, the piezo sensor can detect transverse and impact damage due to the significant effect these have on the stiffness of the composite (Fig. 8b). For these two types of damage, there is a leftward shift in frequency of 17.4 Hz and 6 Hz, respectively, compared to the undamaged composite. The longitudinal damage has a minimal effect on the stiffness of the beam at low frequencies, and as a result, no difference was observed.

At higher frequencies (600–800 Hz), a significant difference can be seen between the undamaged and longitudinally damaged composites (Fig. 8c). The more substantial frequency shift at higher frequencies is due to the smaller wavelength of the vibration in the composite. Thus, using sound as a vibration source can increase the sensitivity of damage detection and localization by exciting high frequency modes. In both frequency ranges, the sensor can easily recognize transverse damage, as this type of damage stops wavelength propagation through the entire composite length. The piezoelectric sensor can generate enough voltage without the need for amplification, even under low-magnitude excitation, although amplification could be used to improve the signal-to-noise ratio and signal transmission. A long vibration test was performed to determine the suitability of the sensors for long-term vibration sensing under sound-induced vibrations, to detect transverse damage on the carbon fiber composite beam for 10 000 seconds (Fig. 8d). The sensor showed stable output, with both frequency and amplitude remaining stable throughout the measured period. The long-term stability of the piezo material is expected to be high with proper sensor design and manufacturing.

Multiple sensors enable effective damage localization and precise calculation of stiffness loss for damage detection in

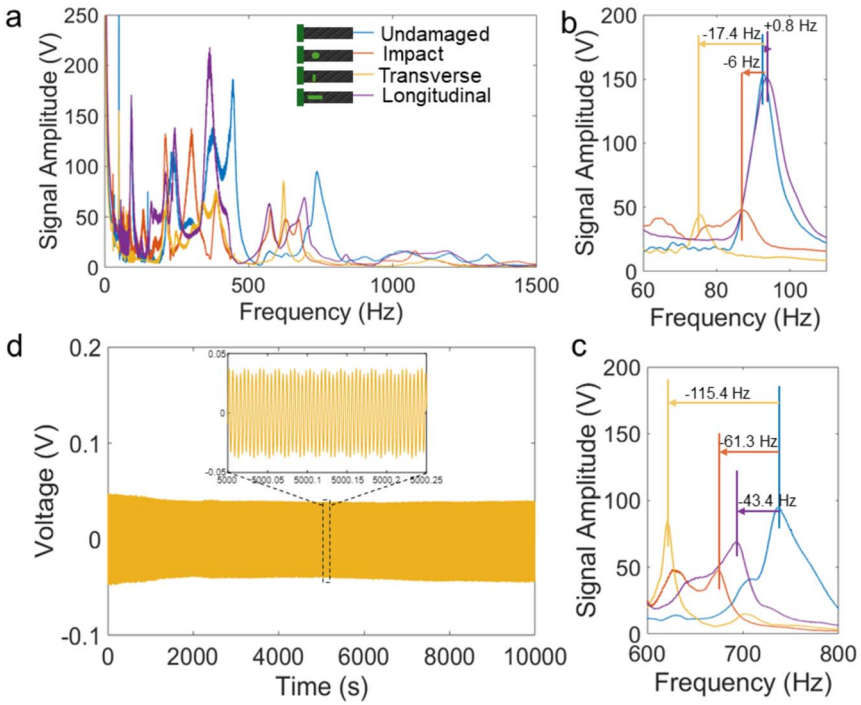

Fig. 8 Frequency spectrum for damaged and undamaged composite beams: (a) entire spectrum and zoomed in view for (b) low frequency and (c) high frequency, and (d) long-term stability test of the piezoelectric sensor (1 wt% AgNPs) in detecting transverse damage in carbon fiber composites.

large structures. Piezoelectric sensors offer the benefit of requiring no external power source. They can detect sound-induced vibrations across a wide frequency range. Advanced signal processing, digital twin analysis, and SHM techniques improve damage detection. This helps prevent catastrophic failures and enables preventative maintenance, increasing safety and extending the lifespan of various structures.

4. Conclusion

In summary, we explored the role of nanofillers of MXenes and AgNPs in enhancing piezoelectric performance of P(VDF-TrFE) for fabricating hybrid piezoelectric sensors through electrospinning. These sensors, for the first time, demonstrate potential in harnessing sound-induced vibrations for *in situ* structural health monitoring of carbon fiber composites. These sensors offer a promising, sustainable and self-powered alternative to traditional accelerometers, which require external power and pose risks in harsh environments. Based on the analysis of the power spectral density factor, carbon fiber composite with a thickness of 0.44 mm was optimized and selected for sensor testing. Carbon fiber composites were subjected to sweep and pink noise tests to compare the performance of the advanced piezo sensor with an accelerometer. The results confirmed the reliability of the signals generated by the flexible piezoelectric sensor, which successfully detected both transverse and impact damage at low frequency ($\leq$100), as well as all types of damage at higher frequencies.

The future application of these sensors in SHM lies within the automotive and aerospace industries, where the high strength and lightweight properties of carbon fiber composites are essential, while simultaneously facing the challenge of sound-induced vibrations. Consequently, these sensors are highly desirable for harnessing this energy to prevent catastrophic failure in a cost-effective approach.

These advanced sensors, by eliminating the need for a power amplifier, have the potential for future smart sensing systems. However, more work is needed to focus on sensor dimensions and electrode design to improve sensitivity and durability for the early detection of non-visible damage in carbon fiber composites. Fatigue monitoring and life cycle assessments need to be considered to ensure the reliability of output results. Integrating these sensors with smart systems and IoT networks will facilitate remote monitoring, enhancing maintenance efficiency in aerospace, automotive, and wind energy applications.

Data availability

The datasets supporting this article have been uploaded as part of the ESI.†

Conflicts of interest

There are no conflicts to declare.

Acknowledgements

F. M. acknowledges financial support received from Deakin University through an Alfred Deakin Postdoctoral Research Fellowship (2022). The authors acknowledge the Deakin University Electron Microscopy facility. R. V. would like to acknowledge the support of the Australian Research Council (DP220100130 and IH210100023) for partial funding of this research.

References

1 N. L. T. Nguyen, C. Creighton, S. Nunna, M. Maghe, T. Groetsch and R. J. Varley, *Polym. Degrad. Stab.*, 2024, **227**, 110835.
2 P. Heidarian, F. Mokhtari, M. Naebe, L. C. Henderson and R. J. Varley, *Resour., Conserv. Recycl.*, 2024, **203**, 107465.
3 S. Y. Oh, D. Lee and Y.-B. Park, *Int. J. Mech. Sci.*, 2024, **281**, 109511.
4 F. Ren, I. N. Giannakeas, Z. Sharif Khodaei and M. H. F. Aliabadi, *NDT&E Int.*, 2024, **141**, 102988.
5 L. Parida and S. Moharana, *Results Eng.*, 2023, **18**, 101093.
6 G. Aranguren, P. Monje, V. Cokonaj, E. Barrera and M. Ruiz, *Rev. Sci. Instrum.*, 2013, **84**, 125106.
7 J. Smithard, N. Rajic, S. Van der Velden, P. Norman, C. Rosalie, S. Galea, H. Mei, B. Lin and V. Giurgiutiu, *Materials*, 2017, **10**, 832.
8 A. P. Strong, N. Sanderson, G. Lees, A. Hartog, R. Twohig, K. Kader, G. Hilton and A. Khlybov, *7th International Pipeline Conference*, Paper No: IPC2008-64549, 2008, pp. 711–719.
9 S. W. Doebling, C. R. Farrar and M. B. Prime, *Shock. Vib. Dig.*, 1998, **30**, 91–105.
10 Y. Han, L. He, X. Zheng, R. Hu, H. Huang and H. Zhao, *Energy Convers. Manage.*, 2023, **286**, 117040.
11 F. Mokhtari, Z. Cheng, C. H. Wang and J. Foroughi, *Glob. Chall.*, 2023, **7**, 2300019.
12 F. Mokhtari, A. Samadi, A. O. Rashed, X. Li, J. M. Razal, L. Kong, R. J. Varley and S. Zhao, *Prog. Mater. Sci.*, 2025, **148**, 101376.
13 F. Mokhtari, H. Y. Nam, A. Ruhparwar, R. Raad, J. M. Razal, R. J. Varley, C. H. Wang and J. Foroughi, *J. Mater. Chem. B*, 2024, **12**, 9727–9739.
14 J. N. Eiras, L. Gavérina and J.-M. Roche, *Sensors*, 2024, **24**, 450.
15 I. Izhar, M. Iqbal and F. Khan, *Energy Convers. Manage.*, 2023, **277**, 116635.
16 Q. Feng and Y. Liang, *Earthquake Res. Adv.*, 2023, **3**, 100154.
17 Y. Bai, C. Xiao, Z. Wei and L. Yin, *J. Phys.: Conf. Ser.*, 2023, **2479**, 012022.
18 O. M. Haid, A. A. M. Ralib, R. A. Rahim, M. A. M. Hatta and F. B. Ahmad, *J. Mater. Chem. B*, 2024, **12**, 9727–9739.
19 Y. Yang, Y. Zhang and X. Tan, *Symmetry*, 2021, **13**, 1998.
20 B. Chen, Y. Jia, F. Narita, H. Kurita and Y. Shi, *Composites, Part B*, 2024, **273**, 111274.
21 D. S. Aulakh and S. Bhalla, *Mech. Syst. Signal Process.*, 2023, **194**, 110272.

22 É. Oliveira, N. Maia, A. Marto, R. Da Silva, F. Afonso and A. Suleman, *Mech. Syst. Signal Process.*, 2016, **79**, 16–29.
23 T. Bregar, B. Starc, G. Čepon and M. Boltežar, *Conference Proceedings of the Society for Experimental Mechanics Series ((CPSEMS)), On the Use of PVDF Sensors for Experimental Modal Analysis*, Cham, 2021, pp. 279–281.
24 F. Mokhtari, S. Danti, B. Azimi, F. Hellies, E. Zanoletti, G. Albertin, L. Astolfi, R. J. Varley and J. M. Razal, *Energy Environ. Mater.*, 2024, e12807.
25 X. Zhu and H. Hao, *Front. Struct. Civ. Eng.*, 2012, **6**, 321–333.
26 F. Mokhtari, Z. Cheng, R. Raad, J. Xi and J. Foroughi, *J. Mater. Chem. A*, 2020, **8**, 9496–9522.
27 M. Kubin, P. Makreski, M. Zanoni, G. Selleri, L. Gasperini, D. Fabiani, C. Gualandi and A. Bužarovska, *Polym. Compos.*, 2023, **44**, 7804–7816.
28 P. M. Ferreira, M. A. Machado, M. S. Carvalho, P. Vilaça, G. Sorger, J. V. Pinto, J. Deuermeier and C. Vidal, *Mater. Charact.*, 2023, **205**, 113371.
29 F. Mokhtari, M. Shamshirsaz, M. Latifi and S. Asadi, *J. Text. Inst.*, 2017, **108**, 906–914.
30 A. Thakur, B. S. Nithin Chandran, K. Davidson, A. Bedford, H. Fang, Y. Im, V. Kanduri, B. C. Wyatt, S. K. Nemani, V. Poliukhova, R. Kumar, Z. Fakhraai and B. Anasori, *Small Methods*, 2023, **7**, 2300030.
31 J. Yun, J. Park, M. Ryoo, N. Kitchamsetti, T. S. Goh and D. Kim, *Nano Energy*, 2023, **105**, 108018.
32 V. A. Cao, M. Kim, S. Lee, C. G. Kim, P. Cao Van, T. N. Thi, J.-R. Jeong and J. Nah, *ACS Appl. Mater. Interfaces*, 2022, **14**, 26824–26832.
33 R. Han, L. Zheng, G. Li, G. Chen, S. Ma, S. Cai and Y. Li, *ACS Appl. Mater. Interfaces*, 2021, **13**, 46738–46748.
34 N. A. Shepelin, P. C. Sherrell, E. N. Skountzos, E. Goudeli, J. Zhang, V. C. Lussini, B. Imtiaz, K. A. S. Usman, G. W. Dicinoski and J. G. Shapter, *Nat. Commun.*, 2021, **12**, 3171.
35 C. T. Pan, K. Dutt, A. Kumar, R. Kumar, C. H. Chuang, Y. T. Lo, Z. H. Wen, C. S. Wang and S. W. Kuo, *Int. J. Bioprint.*, 2023, **9**, 647.
36 S. Asgari, G. Mohammadi Ziarani, A. Badiei and S. Iravani, *Mater. Adv.*, 2023, **4**, 6092–6117.
37 Y. Zhang, M. Wu, Q. Zhu, F. Wang, H. Su, H. Li, C. Diao, H. Zheng, Y. Wu and Z. L. Wang, *Adv. Funct. Mater.*, 2019, **29**, 1904259.
38 M. Yuan, W. Yao, Z. Ding, J. Li, B. Dai, X. Zhang and Y. Xie, *Nano Energy*, 2024, **122**, 109328.
39 P. C. Sherrell, A. Šutka, M. Timusk and A. Šutka, *Small*, 2024, 2311570.
40 F. Mokhtari, K. A. S. Usman, J. Zhang, R. Komljenovic, Ž. Simon, B. Dharmasiri, A. Rezk, P. C. Sherrell, L. C. Henderson, R. J. Varley and J. M. Razal, *ACS Appl. Mater. Interfaces*, 2025, **17**(2), 3214–3228.
41 S. Seyedin, J. Zhang, K. A. S. Usman, S. Qin, A. M. Glushenkov, E. R. S. Yanza, R. T. Jones and J. M. Razal, *Glob. Chall.*, 2019, **3**, 1900037.
42 X. Liu, J. Tong, J. Wang, S. Lu, D. Yang, H. Li, C. Liu and Y. Song, *J. Mater. Chem. C*, 2023, **11**, 4614–4622.
43 L. Paralı, F. Tatardar, M. Koç, A. Sarı and R. Moradi, *J. Mater. Sci.: Mater. Electron.*, 2023, **35**, 41.
44 M. Anayee, *Mechanism and Kinetics of 2D Transition Metal Carbides (MXenes) Synthesis*, Drexel University, 2023.
45 A. Mankuni and S. Varghese, *ACS Appl. Electron. Mater.*, 2024, **6**, 4194–4203.
46 A. Dehingia, U. Das, H. P. Gogoi, K. K. Borgohain, S. Patra, B. Paul and A. Roy, *Small*, 2024, **20**, 2401179.
47 N. Alnairat, M. Abu Dalo, R. Abu-Zurayk, S. Abu Mallouh, F. Odeh and A. Al Bawab, *Polymers*, 2021, **13**, 3683.
48 Y. Li, B. Zhou, Y. Shen, C. He, B. Wang, C. Liu, Y. Feng and C. Shen, *Composites, Part B*, 2021, **217**, 108902.
49 Y. Zhen, V. S. Reddy, B. Ramasubramanian and S. Ramakrishna, *J. Mater. Sci.*, 2022, **57**, 21960–21979.
50 K. Rajavel, S. Luo, Y. Wan, X. Yu, Y. Hu, P. Zhu, R. Sun and C. Wong, *Composites, Part A*, 2020, **129**, 105693.
51 M. I. H. Protyai and A. Bin Rashid, *Heliyon*, 2024, **10**, e37030.
52 J. Deng, P. Zhao, Z. Wu and Y. Wang, *Ceram. Int.*, 2024, **50**, 31154–31163.
53 J. Fan, R. Yang, Y. Du, F. Wang, L. Wang, J. Yang and A. Zhou, *Nano Energy*, 2024, **129**, 109999.
54 R. Atif, J. Khaliq, M. Combrinck, A. H. Hassanin, N. Shehata, E. Elnabawy and I. Shyha, *Polymers*, 2020, **12**, 1304.
55 A. Akbarinejad, H. Fiedler, J. Nguyen, Z. Li, D. A. Gito, P. C. Sherrell, A. V. Ellis, K. Aw and J. Malmstrom, *Adv. Electron. Mater.*, 2024, **10**, 2400019.
56 S. Zhang, T. Jiang, M. Li, H. Sun, H. Wu, W. Wu, Y. Li and H. Jiang, *Nano Energy*, 2024, **131**, 110214.
57 H. Zhang, S. Feng, D. He, P. Molinié and J. Bai, *Nano Energy*, 2019, **63**, 103856.
58 A. Sultana, M. M. Alam, E. Pavlopoulou, E. Solano, M. Berggren, X. Crispin and D. Zhao, *Chem. Mater.*, 2023, **35**, 1568–1578.
59 J.-H. Lee, K. Cho and J.-K. Kim, *Adv. Mater.*, 2024, **36**, 2310505.
60 L. Persano, A. Camposeo, F. Matino, R. Wang, T. Natarajan, Q. Li, M. Pan, Y. Su, S. Kar-Narayan, F. Auricchio, G. Scalet, C. Bowen, X. Wang and D. Pisignano, *Adv. Mater.*, 2024, **36**, 2405363.
61 R. W. Symes, R. J. Varley, N. S. John, M. Ibrahim and M. W. Joosten, *Measurement*, 2025, **242**, 115963.
62 S. Hassani, M. Mousavi and Z. Sharif-Khodaei, in *The Rise of Smart Cities*, ed. A. H. Alavi, M. Q. Feng, P. Jiao and Z. Sharif-Khodaei, Butterworth-Heinemann, 2022, pp. 343–372, DOI: 10.1016/B978-0-12-817784-6.00007-2.
63 Z. He, W. Li, H. Salehi, H. Zhang, H. Zhou and P. Jiao, *Autom. Constr.*, 2022, **136**, 104168.
64 Q. Li, Y. He, K. Zhou, X. Han, Y. He and Z. Shu, *Struct. Des. Tall Build.*, 2018, **27**, e1490.
65 J. Su, Y. Xia and S. Weng, *Struct. Control Health Monit.*, 2020, **27**, e2629.
66 T.-H. Yi, Y. Lei, H.-P. Chen, X.-W. Ye, F. Kang and H. Wang, *Sci. World J.*, 2014, **2014**, 976927.
67 W. Baker, I. McKenzie and R. Jones, *Compos. Struct.*, 2004, **66**, 133–143.
68 M. A. Notarangelo, D. Gargaro, G. Fabbrocino and C. Rainieri, *Proceedings of the 10th International Operational Modal Analysis Conference (IOMAC 2024)*, 2024.

